H2-K^b and H2-D^b regulate cerebellar long-term depression and limit motor learning

Michael J. McConnell[1,2], Yanhua H. Huang[1,3], Akash Datwani, and Carla J. Shatz[3,4]

Bio-X and Departments of Biology and Neurobiology, Stanford University, Stanford, CA 94305

Contributed by Carla J. Shatz, February 24, 2009 (sent for review February 19, 2009)

There are more than 50 class I MHC (MHCI) molecules in the mouse genome, some of which are now known to be expressed in neurons; however, the role of classical MHCI molecules in synaptic plasticity is unknown. We report that the classical MHCI molecules, H2-K^b and H2-D^b, are co-expressed by Purkinje cells (PCs). In the cerebellum of mice deficient for both H2-K^b and H2-D^b (K^{b}D$^{b-/-}$), there is a lower threshold for induction of long-term depression (LTD) at parallel fiber to PC synapses. This change may be a result of additional glutamate release observed at K^{b}D$^{b-/-}$ CF to PC synapses, which are thought to "train" the cerebellar circuit. A behavioral correlate of cerebellar LTD is motor learning; acquisition and retention of a Rotarod behavioral task is significantly better in K^{b}D$^{b-/-}$ mice than in WT cohorts. These physiological and behavioral phenotypes in K^{b}D$^{b-/-}$ mice reveal a surprising role for classical MHCI molecules in synaptic plasticity and motor learning.

cerebellum | neuronal MHC class 1 | synaptic plasticity

The class I MHC (MHCI) locus encodes perhaps the most highly polymorphic gene family in natural populations (1, 2). Although MHCI was not thought to be expressed in the healthy brain, recent discoveries have reported both classical and nonclassical MHCI expression in subsets of neurons, including cerebral cortex, hippocampus (3, 4), motoneurons (5), and the mouse vomeronasal organ (6, 7). MHCI protein has been localized in neuronal dendrites and synapses (3, 8), and the non-classical H2-M10 family is co-expressed with the V2R pheromone receptors (6, 7), possibly related to MHCI-binding peptides, which have been linked to social recognition (9). Initial efforts to explore the function of MHCI in the CNS and olfactory bulb used β2m- and/or TAP1-deficient mice, which have markedly reduced cell surface expression of many, if not all, MHCI molecules (10, 11). These studies implicate neuronal MHCI in activity-dependent synaptic plasticity in visual and hippocampal circuits (4, 8). Additional studies of β2m$^{-/-}$ mice have revealed that the stability of inhibitory synapses onto spinal motor neurons is altered after axotomy (12), and these mice also have defects in pheromone receptor localization and male-male aggressive behavior (7). Initial studies provided support—albeit indirectly—for the idea that neural MHCI molecules have nervous system functions in behavior and plasticity. To obtain direct evidence, studies of mice lacking specific MHCI molecules are needed. Here we report that Purkinje cells (PCs) co-express H2-K^b and H2-D^b, the 2 classical MHCI molecules in C57BL/6 mice. Mice lacking both H2-K^b and H2-D^b (K^{b}D$^{b-/-}$) have phenotypes consistent with a requirement for these specific MHCI molecules in normal cerebellar synaptic plasticity and motor learning.

Results

MHCI Molecules H2-K^b and H2-D^b are Co-Expressed in PCs. Isotopic in situ hybridization (ISH) is extremely sensitive and can be used reliably to detect low-abundance mRNA. RNA probes were designed to recognize distinct regions of *H2-D^b* and *H2-K^b* (4); these detect *H2-K^b* and *H2-D^b* transcripts in the PC layer of C57BL/6 mice (Fig. 1 *A*, *B*, and *D*). No transcripts were detected in K^{b}D$^{b-/-}$ mice (Fig. 1 *C* and *E*). Silver grains marking the exact location of isotopic probes were localized around most large pale nuclei, indicative of PC expression of both transcripts (Fig. 1 *F* and *G*). FISH confirmed co-expression of these transcripts in >80% of PCs (Fig. 1 *H*, *I*, and *J*). MHCI protein can also be detected in PC somata and throughout the cerebellar molecular layer, particularly in the proximal dendrites of PCs (Fig. 1*K*). No staining was observed in control sections (Fig. 1*L*). As expected from the absence of H2-K^b and H2-D^b transcripts (Fig. 1 *C* and *E*), the absence of H2-K^b and H2-D^b proteins in K^{b}D$^{b-/-}$ mice, established previously (13), was confirmed using this antibody [supporting information (SI) Fig. S1].

Normal Development of the K^{b}D$^{b-/-}$ Cerebellum. Neural activity during development is required for normal elimination of supernumerary climbing fiber (CF) axons (14, 15). Given the observation that MHCI transcripts are detected in PCs by postnatal d 7 (Fig. S2 *A* and *B*) and that the retinogeniculate projection fails to undergo normal synapse elimination in β2m$^{-/-}$TAP1$^{-/-}$ mice (4), we examined CF synapse elimination in K^{b}D$^{b-/-}$ mice.

By the end of the third postnatal week, supernumerary CF axons have been eliminated, leaving mostly 1 CF per PC (16, 17). In the cerebellar molecular layer, only CF presynaptic nerve terminals are immunoreactive for vesicular glutamate transporter 2 (vGluT2) (18, 19). Immunostaining for vGluT2 was used to assess the overall density and distribution of CF synapses; no difference between WT and K^{b}D$^{b-/-}$ was found (Fig. 2 *A* and *B* and Fig. S2 *C–E*). To determine if PCs in K^{b}D$^{b-/-}$ mice are singly innervated, CF excitatory postsynaptic currents (EPSCs) were recorded from PCs in the vermis cerebellum using whole-cell voltage-clamp technique. The number of CFs innervating a given PC was estimated by counting the number of discrete EPSC steps (see *Materials and Methods*). Consistent with previous observations (20), 30/31 WT PCs (postnatal d 19–21) had a single, sharp EPSC threshold (Fig. 2*C*). Similar results were obtained in age-matched K^{b}D$^{b-/-}$ mice (i.e., 29/31 PCs had 1 sharp EPSC; Fig. 2*D*). These observations indicate that CF synapse elimination has proceeded normally on K^{b}D$^{b-/-}$ PCs located in the cerebellar vermis. Moreover, Sholl analysis indicates that WT and K^{b}D$^{b-/-}$ PC dendritic arbors are indistinguishable (Fig. S2 *F–H*), leading to the conclusion that cerebellar development is grossly normal in K^{b}D$^{b-/-}$ mice.

Lower Induction Threshold for LTD in Mutant Mice. Even if synapse elimination during development is intact, it is possible that

Author contributions: M.J.M., Y.H.H., and C.J.S. designed research; M.J.M., Y.H.H., and A.D. performed research; M.J.M. contributed new reagents/analytic tools; M.J.M., Y.H.H., and C.J.S. analyzed data; and M.J.M., Y.H.H., and C.J.S. wrote the paper.

The authors declare no conflict of interest.

[1]M.J.M. and Y.H.H. contributed equally to this work.

[2]Present address: Crick-Jacobs Center for Theoretical and Computational Biology, Salk Institute for Biological Studies, La Jolla, CA 92037.

[3]Present address: Program in Neuroscience, Department of Veterinary and Comparative Anatomy, Pharmacology and Physiology, Washington State University, Pullman, WA 99164.

[4]To whom correspondence should be addressed. E-mail: cshatz@stanford.edu.

This article contains supporting information online at www.pnas.org/cgi/content/full/0902018106/DCSupplemental.

www.pnas.org/cgi/doi/10.1073/pnas.0902018106

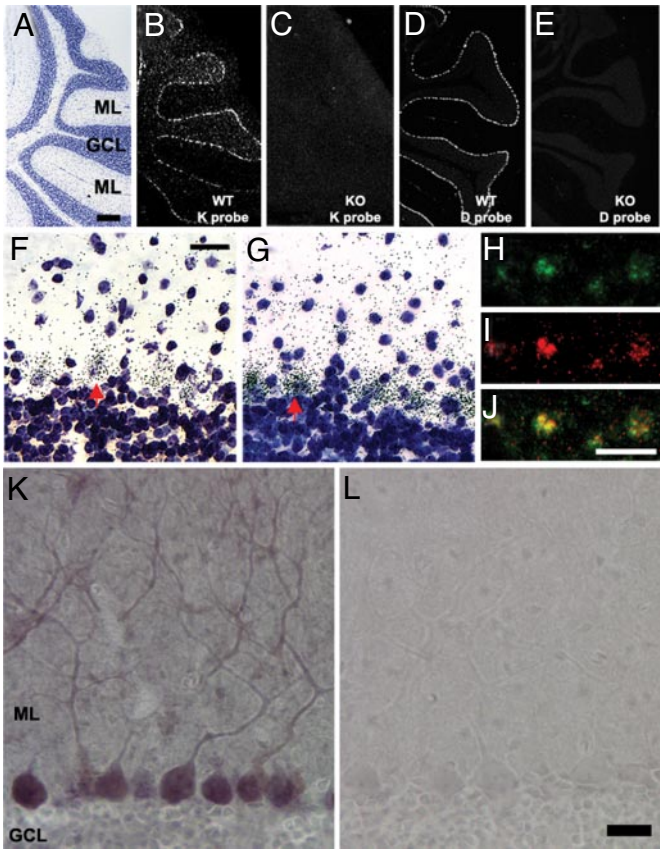

Fig. 1. H2-K^b and H2-D^b are co-expressed in Purkinje neurons. (*A*) Cresyl violet staining (sagittal section at level of cerebellar vermis in adult mouse) shows lobules VI to VIII. The PC layer is located at interface of granule cell layer (*GCL*) and the molecular layer (*ML*). (Scale bar, 400 μm for *A–E*.) (*B*) Hybridization pattern obtained with H2-K^b riboprobe indicates expression in PC layer (isotopic ISH viewed with dark-field optics). (*C*) No hybridization of H2-K^b riboprobe is observed in K^{b}D$^{b-/-}$ cerebellum. (*D*) Hybridization pattern obtained with H2-D^b riboprobe indicates expression of H2-D^b in PC layer. (*E*) No hybridization of H2-D^b riboprobe is observed in K^{b}D$^{b-/-}$ cerebellum. (*F* and *G*) Bright-field images (magnification, ×40) of cresyl violet-counterstained sections show dense H2-K^b (*F*) or H2-D^b (*G*) riboprobe hybridization (small black dots are silver grains) around large pale nuclei in the PC layer (e.g., red arrow). (Scale bar, 20 μm.) (*H-J*) FISH for H2-K^b or H2-D^b: fluorescent micrographs of hapten-labeled H2-K^b riboprobe (*H*, green) or H2-D^b riboprobe (*I*, red) in PC layer; (*J*) merged image of *H* and *I* shows co-localization (yellow) of H2-K^b and H2-D^b riboprobes. (Scale bar, 20 μm.) (*K* and *L*) Immunochemistry detects MHCI protein in PC dendrites and throughout the ML (*K*) but not in IgG-treated control sections (*L*). (Scale bar, 20 μm.)

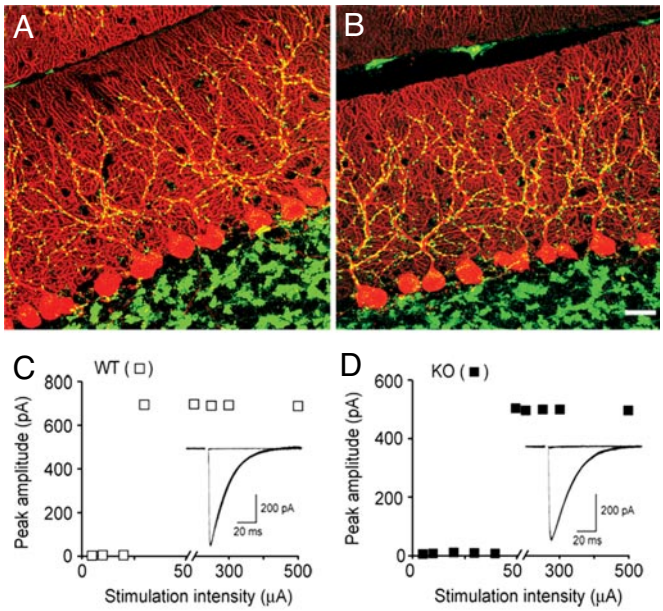

Fig. 2. Developmental regression of CF axons is normal in K^{b}D$^{b-/-}$ mice. (*A* and *B*) PCs are immunostained for calbindin (red) and CF synapses are immunostained for vGluT2 (green) in representative confocal image stacks from postnatal d 21 to 23 WT (*A*) and K^{b}D$^{b-/-}$ (*B*) cerebellum. (Scale bar, 20 μm.) (*C*) Whole-cell voltage-clamp recordings of CF EPSCs from a WT PC of a postnatal d 19 mouse show innervation by a single CF, and corresponding plots of EPSC peak amplitude as a function of stimulus intensity. (*D*) Representative traces and corresponding peak amplitude plots from a postnatal d 21 K^{b}D$^{b-/-}$ PC show single CF innervation. (Holding potential, −15 mV.)

synaptic plasticity is abnormal in mature K^{b}D$^{b-/-}$ mice. We tested if H2-K^b and/or H2-D^b contribute to the development of long-term depression (LTD) at parallel fiber (PF) to PC synapses. PF LTD can be induced by pairing PF stimulation with strong postsynaptic PC depolarization (Fig. 3*A*), or by pairing PF stimulation with direct CF activation (Fig. 3*C*; for review, see ref. 21). Compared with direct CF activation, a strong postsynaptic depolarization of PCs allows more Ca^{2+} influx, which, at high concentrations, facilitates induction of LTD (22).

We first paired bursts of PF stimulation with PC postsynaptic depolarization. In WT animals, PF EPSC amplitude was reduced to 68% ± 4% of baseline level (at 30 min post-induction; Fig. 3*B*), comparable to the amount of depression reported at this synapse using similar protocols (23, 24). In K^{b}D$^{b-/-}$ animals, the same pairing protocol reduced PF EPSCs similarly, to 66% ± 6% of baseline levels (Fig. 3*B*). In either WT or K^{b}D$^{b-/-}$ animals, LTD was not associated with an increase in series resistance during recordings or with a change in the paired-pulse ratio following LTD induction (data not shown). These results suggest that LTD at PF-PC synapses can be induced and can reach a similar level in K^{b}D$^{b-/-}$ animals.

Pairing of PF activation with postsynaptic depolarization bypasses the CF input during LTD induction. However, CF activity critically regulates dendritic Ca^{2+} transients in PCs, and different size Ca^{2+} transients are known to elicit different forms of plasticity ranging from LTD to long-term potentiation (22). We assessed PF-PC LTD by using 2 protocols involving CF input. In the first, CF and PF were co-stimulated at 1 Hz for 300 times (Fig. 3*D*). In the second, to reduce the overall activation of CF synapses, a single CF stimulation followed a burst of PF stimuli repeated 30 times every 15 seconds (Fig. 3*E*).

The co-stimulation protocol (1 Hz, 300 times) leads to a slowly developing LTD (21). In both WT and K^{b}D$^{b-/-}$, the maximal level of LTD (≈60% of baseline) was observed by 40 min post-induction (Fig. 3*D*), similar to previous observations (21, 25). However, significantly more depression was observed in the K^{b}D$^{b-/-}$ cerebellum immediately after induction ($P < 0.05$ at 6, 7, and 8 min). The additional depression observed at 6, 7, and 8 min after induction is probably a result of postsynaptic modifications associated with LTD rather than transient presynaptic changes; the paired-pulse ratio (PPR) of WT and K^{b}D$^{b-/-}$ PF EPSCs during this period was similarly increased, relative to baseline, during this period (WT vs. K^{b}D$^{b-/-}$, $P = 0.649$ at 6 min, $P = 0.305$ at 7 min, and $P = 0.295$ at 8 min).

We then adopted a protocol that involves less overall CF stimulation. CF was stimulated 30 times every 15 seconds, with each round preceded by a short burst of PF stimulation (10 pulses at 100 Hz). In WT animals, PF EPSCs were significantly potentiated immediately after induction (124% ± 7% of baseline at 6 min, $P < 0.01$), but gradually decreased to 87% ± 6% of

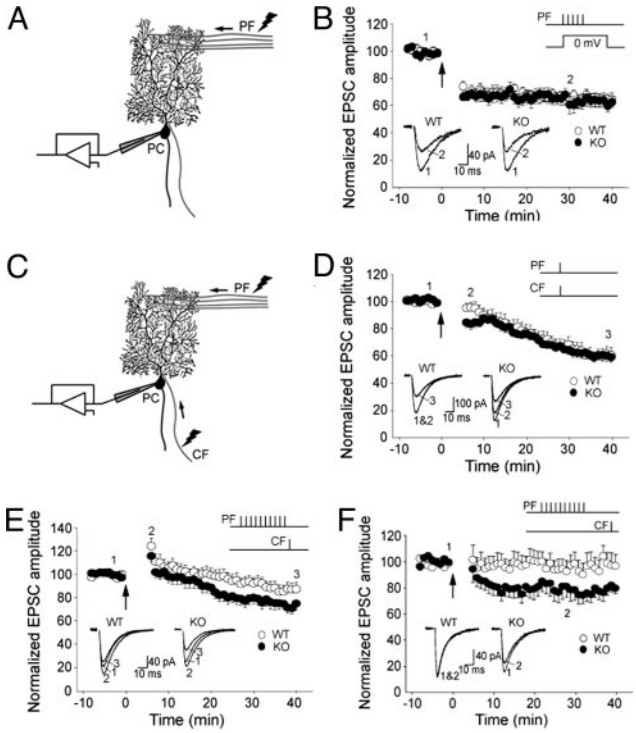

Fig. 3. LTD at PF-PC synapses has lower induction threshold in $K^bD^{b-/-}$ mice. (*A*) Diagram shows the recording configuration for *B*, where PC depolarization is paired with PF stimulation. (*B*) LTD of PF EPSCs can be induced and can reach a similar level in WT ($n = 13$) and $K^bD^{b-/-}$ ($n = 12$) cells ($P = 0.768$ at 30 min post-induction) by pairing presynaptic PF stimulation trains (5 stimuli at 100 Hz) with postsynaptic depolarization (to 0 mV; 100 ms) every 15 sec for 5 min, in voltage-clamp mode using cesium-based internal solution. (*C*) Diagram showing the recording configuration for induction protocols in *D*–*F*, where both CF and PF are stimulated. (*D*) LTD induced in $K^bD^{b-/-}$ ($n = 11$) and WT ($n = 13$) cells ($P < 0.05$ at 6, 7, and 8 min) by conjunctional PF and CF activation at 1 Hz for 5 min, in current-clamp mode (at approximately −70 mV) using potassium-based internal solution. (*E*) LTD induced in $K^bD^{b-/-}$ ($n = 14$) and WT ($n = 13$) cells ($P < 0.05$ at 30 min) by pairing presynaptic PF stimulation trains (10 stimuli at 100 Hz) with single CF activation (10 ms following PF train) every 15 sec for a total of 30 times, in current-clamp mode (at approximately −70 mV) using potassium-based internal solution. Recordings were made at room temperature. (*F*) LTD was induced in $K^bD^{b-/-}$ ($n = 13$) and WT ($n = 14$) cells ($P < 0.05$ at 30 min post-induction) by pairing presynaptic PF stimulation trains (10 stimuli at 100 Hz) with single CF activation (50 ms following PF train) at 0.1 Hz for 5 min, in current-clamp mode (at approximately −70 mV) using potassium-based internal solution. Recordings were made at 31 °C to 33 °C. Bar graphs in *B*, *D*–*F* (*Upper Insets*) indicate the specific induction protocols. Arrows indicate the starting points of the ~5 min inductions. Traces (*Lower Inset*) show example averaged EPSCs (8–12 consecutive responses) taken at the times indicated by the numbers on the graphs.

baseline by 30 min post-induction (Fig. 3*E*). The initial potentiation was accompanied by a transient but significant decrease in PPR (81% ± 2% of baseline, $P < 0.001$) and thus may be of mainly presynaptic origin. In $K^bD^{b-/-}$ mice, this protocol induced a similar initial potentiation (116% ± 5% of baseline at 6 min, $P = 0.421$ vs. WT; PPR, 82% ± 2% of baseline) followed by a slow-developing LTD, but the LTD was notably more pronounced: 71% ± 5% of baseline by 30 min post-induction ($P < 0.05$; Fig. 3*E*). The percentage change of PPR during the course, relative to baseline, was not significantly different between WT and $K^bD^{b-/-}$ animals ($P = 0.136$ at 30 min post-induction). Finally, the induction threshold for $K^bD^{b-/-}$ PF LTD was also lower when using a similar induction protocol at 32 °C (Fig. 3*F*). Taken together, induction protocols that include CF stimulation reveal a significantly lower threshold for PF LTD in $K^bD^{b-/-}$ mice than in WT controls.

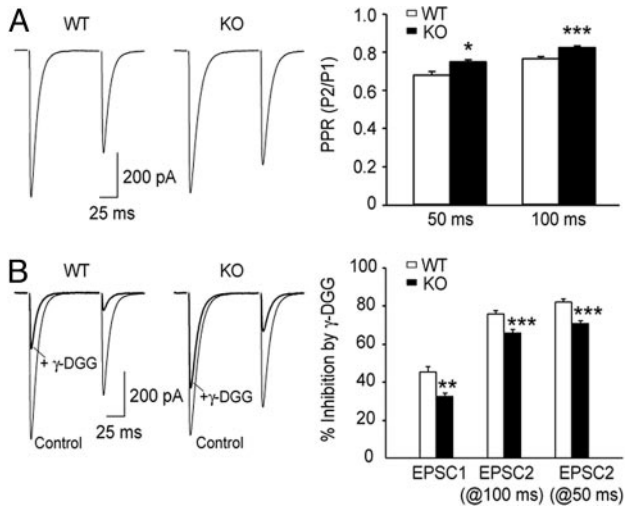

Fig. 4. CF EPSCs have reduced paired-pulse depression and decreased sensitivity to γ-DGG in $K^bD^{b-/-}$ mice. (*A*) Example traces of paired CF EPSCs from a WT and a $K^bD^{b-/-}$ mouse, and grouped data show the mean PPR (i.e., peak amplitude of EPSC2/EPSC1; *P2/P1*) at 50 ms ($n = 8$ WT cells; $n = 11$ $K^bD^{b-/-}$ cells) and 100 ms inter-stimulus intervals (ISIs; $n = 11$ WT cells; $n = 16$ $K^bD^{b-/-}$ cells) in the 2 genotypes (at 50-ms ISI: WT, 0.68 ± 0.02; $K^bD^{b-/-}$, 0.75 ± 0.01; at 100-ms ISI: WT, 0.767 ± 0.009; $K^bD^{b-/-}$, 0.826 ± 0.008); $^*P < 0.05$; $^{***}P < 0.001$. CF EPSCs recorded under voltage-clamp mode at the holding potential of −10 mV were not significantly different from WT control animals (Table S1). (*B*) Example traces of CF EPSCs recorded in the absence and presence of 2 mM γ-DGG, and grouped data show mean percentage inhibition of peak amplitude in the 2 genotypes ($n = 8$ WT cells; EPSC1 = 45.3% ± 2.8%; EPSC2 at 100-ms ISI, 75.8% ± 1.7%; EPSC2 at 50 ms ISI, 82.1% ± 1.5%; $n = 11$ $K^bD^{b-/-}$ cells; EPSC1, 32.5% ± 1.5%; EPSC2 at 100 ms ISI, 65.9% ± 1.7%; EPSC2 at 50 ms ISI, 70.9% ± 1.3%). **, $P < 0.01$. Holding potential was −10 mV.

A Larger Glutamate Transient at CF-PC Synapses in $K^bD^{b-/-}$ Mice. The efficacy of CF synaptic transmission was examined in $K^bD^{b-/-}$ mice. The rise and decay kinetics of $K^bD^{b-/-}$ CF EPSCS are comparable to WT cohorts (Fig. 4*A* and Table S1) and to previous observations (26); CF complex spikes were also indistinguishable between WT and $K^bD^{b-/-}$ mice (Table S2). However, when a pair of stimuli separated by 50 or 100 ms was applied to a CF, the second evoked EPSC (EPSC2) was significantly larger in $K^bD^{b-/-}$ animals, rendering larger PPRs (EPSC2/EPSC1) at $K^bD^{b-/-}$ CF synapses (Fig. 4*A*)

In normal release conditions, it is thought that postsynaptic glutamate receptors are saturated during CF EPSC1 (16, 27, 28) and that the smaller second EPSC reflects depletion of presynaptic vesicles (29). Therefore, the larger EPSC2 observed in $K^bD^{b-/-}$ animals might arise from increased glutamate release from CF terminals; this increase would not be as apparent at EPSC1 as a result of receptor saturation. To determine if more glutamate is released at CF-PC synapses in $K^bD^{b-/-}$ mice, we measured the percentage inhibition of EPSC peak amplitude by the low-affinity, competitive AMPA receptor antagonist γ-D-glutamyl-glycine (γ-DGG). γ-DGG exhibits rapid dissociation kinetics and is able to compete for glutamate binding during transmission (28, 30). It is therefore predicted that a larger glutamate transient would render less inhibition by γ-DGG. Consistent with previous studies (30), γ-DGG (2 mM) reduced the peak amplitude of both EPSC1 and EPSC2 in WT PCs; the greater reduction in EPSC2 suggests a smaller glutamate transient at the second stimulus (Fig. 4*B*). In $K^bD^{b-/-}$ animals, γ-DGG reduced EPSC1 peak amplitude significantly less than that in WT (Fig. 4*B*; 32.5% ± 1.5% inhibition in $K^bD^{b-/-}$ vs. 45.3% ± 2.8% inhibition in WT, $P < 0.01$). At 50 and 100 ms following the first stimulus, EPSC2 was also reduced less in $K^bD^{b-/-}$ animals than in WT (Fig. 4*B*). These results suggest that

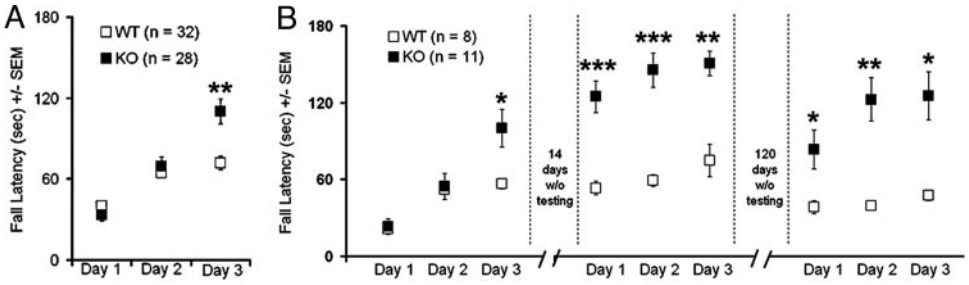

Fig. 5. $K^bD^{b-/-}$ mice outperform WT cohorts on the Rotarod behavioral task. (*A*) Average Rotarod performance on 3 consecutive days (*x* axis) is plotted on the *y* axis for WT (white squares) and $K^bD^{b-/-}$ (black squares) mice. **, $P < 0.005$. (*B*) Average Rotarod performance during three 3-day periods (*x* axis) is plotted on the *y* axis for WT (white squares) and $K^bD^{b-/-}$ (black squares) mice. Fourteen days elapsed between the first and second 3-day periods, 120 d elapsed between the second and third 3-day periods. *, $P < 0.05$; **, $P < 0.005$; ***, $P = 0.0005$. Error bars indicate the SEM on all graphs.

glutamate transients in the CF synaptic cleft, at both the first and second stimuli, are greater in $K^bD^{b-/-}$ animals.

Enhanced Motor Learning and Retention in $K^bD^{b-/-}$ Mice. LTD at PF-PC synapses is thought to underlie several forms of cerebellar-based motor learning (21, 31, 32). To explore possible behavioral correlates, a Rotarod behavioral task (33) was used (Fig. 5). Both WT and $K^bD^{b-/-}$ mice had equivalent performance on day 1 (WT fall latency, 40.3 ± 3.3 s; $K^bD^{b-/-}$ fall latency, 33.4 ± 4.6 s) and significant learning after 1 day of training (WT fall latency, 64.8 ± 3.8 s; $K^bD^{b-/-}$ fall latency, 69.4 ± 6.8 s; $P < 0.0001$ for day 2 vs. day 1). However, by the third day of testing, $K^bD^{b-/-}$ mice significantly outperformed WT cohorts (Fig. 5*A*; WT fall latency, 71.9 ± 4.8 s; $K^bD^{b-/-}$ fall latency, 110.1 ± 9.2 s).

Not only do $K^bD^{b-/-}$ mice outperform WT mice in learning the Rotarod task, they also have impressive retention of this skill. The genotypes of one set of trained mice ($n = 8$ WT; $n = 11$ $K^bD^{b-/-}$) were kept blinded following the initial 3-d testing period for a subsequent period of 4.5 months. Mice performed the 3-d protocol again at 2 more times: after a 2-week rest period and then again after a 4-month rest period. Remarkably, $K^bD^{b-/-}$ mice significantly outperformed WT cohorts on the first day, and on subsequent days, following each rest period (Fig. 5*B*). Improved Rotarod performance and retention are consistent with, but not necessarily caused by, the observed lower threshold LTD induction in $K^bD^{b-/-}$ mice.

Discussion

By examining the patterns of expression of several MHCI mRNAs at different times in development and in adulthood (4), we observed that H2-K^b and H2-D^b are not only expressed in particular subsets of neurons throughout the brain, but as shown here, within the cerebellum they are co-expressed in PCs but not other neurons. Using an antibody known to recognize H2-D^b preferentially (S. Thams and S. Cullheim, personal communication; Fig. S1), immunostaining can be detected in PC somata and along proximal dendrites. Thus, PCs express these classical MHCI molecules (Fig. 1), prompting us to search for specific deficits related to PC morphology, function, or synaptic plasticity in mice lacking H2-K^b and H2-D^b.

A major finding of this study is that H2-K^b and H2-D^b regulate synaptic plasticity in the cerebellum. Using $K^bD^{b-/-}$ mice, we show that these classical MHCI molecules lower the threshold for LTD at PF-PC synapses and limit the extent and retention of motor learning. Previous experiments suggested that MHCI molecules are required for a normal range of synaptic plasticity in hippocampus and for synapse elimination in the visual pathway: mice doubly mutant for β2m and TAP1 have enhanced long-term potentiation and lack LTD in adult hippocampus, and retain an immature pattern of axonal projections from retina to lateral geniculate nucleus (4). However, the conclusion that MHCI is required for these aspects of synaptic plasticity was indirect because β2m and TAP1 are needed for stable cell surface expression of most if not all of the more than 50 MHCI proteins present in the murine genome (10, 11). To our knowledge, alteration of synaptic plasticity or behavior by specific MHCI molecules has not been demonstrated previously.

Improved Motor Learning as a Behavioral Correlate of Lower Threshold LTD. Improved acquisition and retention of Rotarod performance, as observed in $K^bD^{b-/-}$ mice, is quite notable in several respects. Motor learning is thought to be mediated by the cerebellar microcircuit. Patterned neural output is relayed to PCs through PFs; in turn, PCs provide inhibitory modulation of outgoing motor commands. Learning occurs when error signals (e.g., a misstep on a rotating rod) are conveyed to PCs via CFs (for review, see refs. 21, 31, 32). Conjunctive stimulation of both CF-PC and PF-PC synapses depresses "erroneous" PF–PC synapses, thereby training the circuit to minimize output errors. It follows that impaired PF LTD should diminish motor learning, whereas more robust PF LTD would improve motor learning. Several mutant mice with diminished cerebellar LTD do display impaired motor learning (34–36).

Here, the inverse correlation is demonstrated in $K^bD^{b-/-}$ mice: lower threshold cerebellar LTD (Fig. 3) is associated with improved motor learning (Fig. 5). The change in cerebellar LTD observed in $K^bD^{b-/-}$ mice is distinct from the other known example of enhanced LTD in $FMR1^{-/-}$ mutant mice (37); LTD in these mice is increased in magnitude, rather than lower in threshold. This difference may result from what is thought to be a cell-autonomous effect of FMR1 deficiency on local protein translation within the PCs (37), rather than increased CF glutamate release as observed in $K^bD^{b-/-}$ mice (Fig. 4; discussed later). Indeed, CF physiology is normal in $FMR1^{-/-}$ mice (37).

Long-term retention of Rotarod performance in $K^bD^{b-/-}$ mice is also a novel phenotype and may indicate additional roles for H2-K^b and/or H2-D^b outside the cerebellar cortex (38, 39). However, neither hyperactivity nor altered anxiety were observed in $K^bD^{b-/-}$ mice (Fig. S3 *A* and *B*). Moreover, although Rotarod performance is a reliable, simple test for gross motor performance, more sophisticated measurements of specific motor circuits (e.g., the vestibulo-ocular reflex) could add resolution to the precise role of H2-K^b and H2-D^b in cerebellar-dependent motor learning.

Immune Compromise Cannot Account for Improved Motor Learning. We believe the motor learning (as well as LTD) phenotypes observed here are most likely a direct consequence of the observed PC expression of H2-K^b and H2-D^b. Nevertheless, it is possible that neural phenotypes might be a secondary consequence of altered functioning of the immune system. $K^bD^{b-/-}$

mice, in which H2-K^b and H2-D^b are absent in all cells of the body including neurons, have a significantly reduced population of CD8$^+$ T cells (40). Similar CD8$^+$ immunodeficiency is observed in β2m$^{-/-}$, TAP1$^{-/-}$, and β2m$^{-/-}$TAP1$^{-/-}$ mutant mice (11); however, these 3 mutants differ in terms of Rotarod performance (Fig. S3*C*). β2m$^{-/-}$TAP1$^{-/-}$ mice, like K^{b}D$^{b-/-}$ mice, show improved Rotarod performance, but this improvement is not observed in either single mutant (Fig. S3*C*). Similarly, other immunocompromised mice, such as CD3$\zeta^{-/-}$ which lack T cells more generally (4), and PirB$^{\Delta/\Delta44}$, in which B cells and dendritic cells are likely abnormal (41), learn the Rotarod task similarly to WT cohorts (Fig. S3*C*). Thus, a direct role for H2-K^b and H2-D^b in cerebellar function, rather than a secondary consequence of compromised immunity, best accounts for the reported phenotypes.

Huh et al. (4) also addressed a possible secondary consequence of immune compromise; it was found that hippocampal synaptic plasticity was altered in β2m$^{-/-}$TAP$^{-/-}$ and CD3$\zeta^{-/-}$ mice, but appeared normal in immunocompromised RAG1$^{-/-}$ mice. Moreover, we report behavioral enhancement in K^{b}D$^{b-/-}$ and β2m$^{-/-}$TAP1$^{-/-}$ mice, whereas SCID mice display impaired synaptic plasticity and learning deficits (42). Transgenic mouse lines designed to obtain neuron-restricted deletion of the H2-K^b and H2-D^b alleles will be required to exclude formally every immunological variable from a role in the CNS phenotypes reported here. Given these considerations, and in view of the neuronal expression patterns of H2-K^b and H2-D^b, we conclude that immunological deficits per se cannot account adequately for enhanced Rotarod performance, nor are they likely to underlie synaptic phenotypes observed in K^{b}D$^{b-/-}$ mice.

Pre- Versus Post-Synaptic MHCI Function. In this study, postsynaptic expression of H2-K^b and H2-D^b in PC dendrites is associated with postsynaptic forms of LTD. However, larger glutamate transients at CF-PC synapses might be most readily explained via presynaptic changes. Although larger transients can result from either increased release from presynaptic nerve terminals or reduced clearance by postsynaptic glutamate transporters, reduced clearance is not thought to change γ-DGG sensitivity at the peak of glutamate transients (43). At PF synapses, we observed increased paired-pulse facilitation in K^{b}D$^{b-/-}$ animals (Fig. S4), also consistent with a presynaptic change.

In canonical MHCI signaling, the membrane-bound MHCI molecule acts as a ligand that interacts with MHCI receptors (i.e., T cell receptor, Ly49, PirB) and initiates signaling cascades in a non-cell-autonomous manner. Whereas functional T cell receptors are not thought to be expressed by neurons (44), neuronal expression of other MHCI receptors including PirB (45), Ly49 (46), and Kir (47) has now been seen. However, in mice with deficiencies affecting known MHCI receptors expressed in neurons (e.g., CD3$\zeta^{-/-}$ and PirB$^{\Delta/\Delta}$; Fig. S3*C*), we observed normal motor learning. It therefore remains to be determined whether there are additional neuronal MHCI receptors in the cerebellum; this is likely given the very large number and diversity of MHCI receptors known to function in innate immunity (48).

A major advance here is the demonstration that cerebellar LTD and motor learning are regulated by H2-K^b and/or H2-D^b, both of which are selectively expressed in PCs. It was not previously known which of the more than 50 MHCI family members might contribute to neuronal phenotypes observed in β2m$^{-/-}$ and/or β2m$^{-/-}$TAP1$^{-/-}$ mice (4, 7, 8, 12). The fact that this large family of molecules is highly polymorphic in natural populations (1, 2), and that the expression pattern of individual family members varies throughout the CNS (4), raises the intriguing possibility that particular MHCI molecules, as well as cognate receptors, may play specific roles in regulating the capacity of distinct brain circuits to change with learning and experience.

Materials and Methods

Animals. K^{b}D$^{b-/-}$ mice, offspring of breeding pairs on a C57BL/6 background generously provided by H. Ploegh (Cambridge, MA) (40, 49), were maintained in a pathogen-free environment. C57BL/6 (i.e., WT) controls were purchased (Charles River). All protocols were approved by the Harvard Medical School and Stanford University Animal Care and Use Committees.

ISH. Isotopic ISH and cresyl violet counterstaining were performed as described previously (44). For FISH, FITC-labeled H2-K^b and digoxigenin-labeled H2-D^b riboprobes were synthesized by in vitro transcription and processed as for isotopic ISH. Additional details can be found in *SI Methods*. All images were obtained using a Nikon E800 fluorescence microscope (Nikon) and Spot digital camera and software (Diagnostic Instruments, Sterling). Unless indicated otherwise, reagents were obtained from Sigma-Aldrich.

Immunohistochemistry. MHCI immunostaining was performed after transcardial perfusion with PBS solution followed by 4% paraformaldehyde. Brains were then removed, postfixed in 4% paraformaldehyde for 2 h at room temperature, and cryoprotected by sinking in 30% sucrose at 4 °C. Sagittal sections (50 μm) at the level of the cerebellar vermis were sliced using a freezing microtome (Microm HM440E; Richard-Allen Scientific). Sections were processed as follows: two 10-min washes in PBS solution, quenching in 0.3% H_2O_2 for 30 min, avidin-biotin blocking (Vector Laboratories), followed by 1 h in 1% blocking reagent (cat. no. T20915; Invitrogen) in PBS solution plus 0.05% Tween 20 (PBS-T). Blocked sections were incubated with 8 μg/mL rat anti-mouse MHCI (ErHr52; BMA Biochemicals) or 8 μg/mL rat IgG2 (MCA1212; AbD Serotec) in 1% blocking reagent for 36 h at 4 °C. After three 30-min washes in PBS-T, sections were incubated with biotinylated goat F(ab′)2 anti-rat (112–066-072; Jackson Immunoresearch) in 1% blocking reagent. Following three 30-min washes in PBS-T, bound antibody was detected using ABC signal amplification (Vector) and diaminobenzidine/nickel staining (Vector). Sections were dehydrated in ethanol and mounted using xylene and Permount. Digital images were obtained using bright-field microscopy (Nikon E800) and Spot digital camera and software (Diagnostic Instruments), and manually adjusted to optimize the dynamic range and sharpness in Photoshop (Adobe Systems); identical adjustments were performed on images of IgG-treated sections. Immunostaining for vGluT2 and calbindin was performed on sections of postnatal d 21 to 23 cerebellum using standard methodology (see *SI Methods*).

Behavioral Studies. All studies were initiated with 8- to 12-week-old male mice and performed blinded to genotype. Weight differences were not observed between genotypes. Motor learning studies were performed by testing mice 3 times per day on each of 3 consecutive days. The Rotarod apparatus (EzRod; Accuscan Instruments) was programmed to accelerate to 15 rpm over 1 min, hold at 15 rpm for 1 min 50 seconds, then decelerate to 0 during the last 10 seconds. Fall latency was measured as the time the mouse remained on the rod or, rarely, until a passive rotation was observed (33). Data were analyzed and graphs were prepared using Excel (Microsoft). Rotarod data were not normally distributed at every time point, so a Wilcoxon rank-sum test was performed in MatLab (Mathworks) for all Rotarod statistics.

Electrophysiology. Parasagittal slices (250 μm) of the cerebellar vermis were prepared from postnatal d 19 to 25 mice as described previously (50). Recordings were made under visual guidance ($\times$40, differential interference contrast optics) with electrodes (3–5 MΩ) filled with (in mM): $CsCH_3O_3S$ (MeS), 105; TEA-Cl, 20; EGTA, 10; Hepes, 20; Mg-ATP, 2; Na-GTP, 0.2; QX-314, 1; pH 7.3 (Fig. 2 *C* and *D*; Fig. 4; Fig. S4; and Table S1); or CsMeS, 120; CsCl, 10; EGTA, 0.5; Hepes, 10; $MgCl_2$, 2; $CaCl_2$, 0.16; Na-ATP, 4; Na-GTP, 0.4; pH 7.3 (Fig. 3*B*); or KMeS, 130; NaCl, 10; EGTA, 0.5; Hepes, 10; $CaCl_2$, 0.16; Mg-ATP, 4; Na-GTP, 0.4; pH 7.3 (Fig. 3 *D*, *E*, and *F* and Table S2). External perfusion artificial CSF (ACSF) contained (in mM): NaCl, 119; KCl, 2.5; $CaCl_2$, 2.5; $MgCl_2$, 1.3; NaH_2PO_4, 1; $NaHCO_3$, 26.2; and glucose, 11; saturated with 95% O_2/5% CO_2; and included SR 95531 (5 μM) to block $GABA_A$ receptors. Series resistance was 8 to 14 MΩ, and was left uncompensated. Series resistance was monitored continuously during all recordings, and a change beyond 20% was not accepted for data analysis. All recordings were made at room temperature unless indicated otherwise.

Excitatory afferents were stimulated by a constant-current isolated stimulator (model 2100; A-M Systems) using a glass pipette filled with ACSF. To search for CFs, stimulating electrode was systematically moved around in the

granule cell layer delivering paired pulses. CF EPSCs were identified by their all-or-none responses and paired-pulse depression. Subthreshold stimulations did not induce EPSCs, indicating no contamination from parallel fiber synapses. To search for multiple CF innervations, the stimulation intensity was then adjusted over the range of 2 to 500 μA. The membrane potential of PCs was held at -65 mV to maximize the detection sensitivity until the EPSCs were beyond voltage control, and then PCs were depolarized to approximately -10 mV to reduce the size of EPSCs to a manageable range. The number of CFs innervating a given PC was estimated by counting the number of discrete EPSC steps as stimulation intensity was gradually increased. Parallel fibers were stimulated in the molecular layer. Trains of pulses were generated using a programmable pulse generator (model 2100; A-M Systems). Stimulus strength was adjusted so that the first EPSC was approximately 100 to 300 pA.

Synaptic currents were recorded with a MultiClamp 700A amplifier (Axon Instruments; Molecular Devices), filtered at 3 kHz, amplified 5 or 10 times, and then digitized at 20 kHz with a Digidata 1322A analog-to-digital converter (Axon Instruments).

For recordings at increased temperatures, ACSF was heated by passing through a feedback-controlled in-line heater (Warner Instruments) before entering the chamber. SR-95531 hydrobromide (gabazine) and γ-DGG were purchased from Tocris Cookson. All other chemicals were purchased from Sigma-Aldrich.

All analyses were performed blinded to genotypes. Data were analyzed off-line using pClamp software (Axon Instruments). Statistical significance was determined using the Student *t* test unless specified otherwise, and mean values are expressed $\pm$ SEM. Stimulus artifacts were blanked from evoked synaptic currents for clarity.

ACKNOWLEDGMENTS. We thank Drs. W. Regher and J. Raymond for critical comments on the manuscript; Drs. P. Safo, S. Brenowitz, M. Carey, M. Paukert, F. Li, and members of the Shatz lab for helpful suggestions; and B. Printseva, C. Daiz, M. Marcotrigiano, J. Neville-Golden, and Drs. A. Fischer and P. Carpentier for technical assistance. This work was supported by National Institutes of Health Grant MH071666 (to C.J.S.) and by Grant T32CA09361 (to M.J.M.), and by the Dana Foundation (C.J.S.). Neurolucida was provided by National Institutes of Health Core Grant P30EY012196 to the Department of Neurobiology of Harvard Medical School.

1. Lefranc MP (2003) IMGT, the international ImMunoGeneTics database. *Nucleic Acids Res* 31:307–310.
2. Duncan WR, Wakeland EK, Klein J (1979) Heterozygosity of H-2 loci in wild mice. *Nature* 281:603–605.
3. Corriveau RA, Huh GS, Shatz CJ (1998) Regulation of class I MHC gene expression in the developing and mature CNS by neural activity. *Neuron* 21:505–520.
4. Huh GS, et al. (2000) Functional requirement for class I MHC in CNS development and plasticity. *Science* 290:2155–2159.
5. Linda H, Hammarberg H, Piehl F, Khademi M, Olsson T (1999) Expression of MHC class I heavy chain and beta2-microglobulin in rat brainstem motoneurons and nigral dopaminergic neurons. *J Neuroimmunol* 101:76–86.
6. Ishii T, Mombaerts P (2008) Expression of nonclassical class I major histocompatibility genes defines a tripartite organization of the mouse vomeronasal system. *J Neurosci* 28:2332–2341.
7. Loconto J, et al. (2003) Functional expression of murine V2R pheromone receptors involves selective association with the M10 and M1 families of MHC class Ib molecules. *Cell* 112:607–618.
8. Goddard CA, Butts DA, Shatz CJ (2007) Regulation of CNS synapses by neuronal MHC class I. *Proc Natl Acad Sci USA* 104:6828–6833.
9. Spehr M, et al. (2006) Essential role of the main olfactory system in social recognition of major histocompatibility complex peptide ligands. *J Neurosci* 26:1961–1970.
10. Machold RP, Andree S, Van Kaer L, Ljunggren HG, Ploegh HL (1995) Peptide influences the folding and intracellular transport of free major histocompatibility complex class I heavy chains. *J Exp Med* 181:1111–1122.
11. Ljunggren HG, et al. (1995) MHC class I expression and CD8+ T cell development in TAP1/beta 2-microglobulin double mutant mice. *Int Immunol* 7:975–984.
12. Oliveira AL, et al. (2004) A role for MHC class I molecules in synaptic plasticity and regeneration of neurons after axotomy. *Proc Natl Acad Sci USA* 101:17843–17848.
13. Perarnau B, et al. (1999) Single H2Kb, H2Db and double H2KbDb knockout mice: Peripheral CD8+ T cell repertoire and anti-lymphocytic choriomeningitis virus cytolytic responses. *Eur* J Immunol 29:1243–1252.
14. Kakizawa S, Yamasaki M, Watanabe M, Kano M (2000) Critical period for activity-dependent synapse elimination in developing cerebellum. *J Neurosci* 20:4954–4961.
15. Andjus PR, Zhu L, Cesa R, Carulli D, Strata P (2003) A change in the pattern of activity affects the developmental regression of the Purkinje cell polyinnervation by climbing fibers in the rat cerebellum. *Neuroscience* 121:563–572.
16. Hashimoto K, Kano M (2003) Functional differentiation of multiple climbing fiber inputs during synapse elimination in the developing cerebellum. *Neuron* 38:785–796.
17. Crepel F (1982) Regression of functional synapses in the immature mammalian cerebellum. *Trends Neurosci* 5:266–269.
18. Hioki H, et al. (2003) Differential distribution of vesicular glutamate transporters in the rat cerebellar cortex. *Neuroscience* 117:1–6.
19. Fremeau RT Jr, et al. (2001) The expression of vesicular glutamate transporters defines two classes of excitatory synapse. *Neuron* 31:247–260.
20. Nishiyama H, Linden DJ (2004) Differential maturation of climbing fiber innervation in cerebellar vermis. *J Neurosci* 24:3926–3932.
21. Ito M (2001) Cerebellar long-term depression: Characterization, signal transduction, and functional roles. *Physiol Rev* 81:1143–1195.
22. Coesmans M, Weber JT, De Zeeuw CI, Hansel C (2004) Bidirectional parallel fiber plasticity in the cerebellum under climbing fiber control. *Neuron* 44:691–700.
23. Brasnjo G, Otis TS (2001) Neuronal glutamate transporters control activation of postsynaptic metabotropic glutamate receptors and influence cerebellar long-term depression. *Neuron* 31:607–616.
24. Shin JH, Linden DJ (2005) An NMDA receptor/nitric oxide cascade is involved in cerebellar LTD but is not localized to the parallel fiber terminal. *J Neurophysiol* 94:4281–4289.
25. Reynolds T, Hartell NA (2000) An evaluation of the synapse specificity of long-term depression induced in rat cerebellar slices. *J Physiol* 527:563–577.
26. Huang YH, Dykes-Hoberg M, Tanaka K, Rothstein JD, Bergles DE (2004) Climbing fiber activation of EAAT4 transporters and kainate receptors in cerebellar Purkinje cells. *J Neurosci* 24:103–111.
27. Harrison J, Jahr CE (2003) Receptor occupancy limits synaptic depression at climbing fiber synapses. *J Neurosci* 23:377–383.
28. Foster KA, Kreitzer AC, Regehr WG (2002) Interaction of postsynaptic receptor saturation with presynaptic mechanisms produces a reliable synapse. *Neuron* 36:1115–1126.
29. Foster KA, Regehr WG (2004) Variance-mean analysis in the presence of a rapid antagonist indicates vesicle depletion underlies depression at the climbing fiber synapse. *Neuron* 43:119–131.
30. Wadiche JI, Jahr CE (2001) Multivesicular release at climbing fiber-Purkinje cell synapses. *Neuron* 32:301–313.
31. Ito M (2000) Mechanisms of motor learning in the cerebellum. *Brain Res* 886:237–245.
32. Jorntell H, Hansel C (2006) Synaptic memories upside down: Bidirectional plasticity at cerebellar parallel fiber-Purkinje cell synapses. *Neuron* 52:227–238.
33. McFadyen MP, Kusek G, Bolivar VJ, Flaherty L (2003) Differences among eight inbred strains of mice in motor ability and motor learning on a rotorod. *Genes Brain Behav* 2:214–219.
34. Kashiwabuchi N, et al. (1995) Impairment of motor coordination, Purkinje cell synapse formation, and cerebellar long-term depression in GluR delta 2 mutant mice. *Cell* 81:245–252.
35. Miyata M, et al. (2001) Deficient long-term synaptic depression in the rostral cerebellum correlated with impaired motor learning in phospholipase C beta4 mutant mice. *Eur J Neurosci* 13:1945–1954.
36. Ichise T, et al. (2000) mGluR1 in cerebellar Purkinje cells essential for long-term depression, synapse elimination, and motor coordination. *Science* 288:1832–1835.
37. Koekkoek SK, et al. (2005) Deletion of FMR1 in Purkinje cells enhances parallel fiber LTD, enlarges spines, and attenuates cerebellar eyelid conditioning in Fragile X syndrome. *Neuron* 47:339–352.
38. van Alphen AM, De Zeeuw CI (2002) Cerebellar LTD facilitates but is not essential for long-term adaptation of the vestibulo-ocular reflex. *Eur J Neurosci* 16:486–490.
39. Boyden ES, Katoh A, Raymond JL (2004) Cerebellum-dependent learning: The role of multiple plasticity mechanisms. *Annu Rev Neurosci* 27:581–609.
40. Vugmeyster Y, et al. (1998) Major histocompatibility complex (MHC) class I KbDb -/- deficient mice possess functional CD8+ T cells and natural killer cells. *Proc Natl Acad Sci USA* 95:12492–12497.
41. Ujike A, et al. (2002) Impaired dendritic cell maturation and increased T(H)2 responses in PIR-B(-/-) mice. *Nat Immunol* 3:542–548.
42. Ziv Y, et al. (2006) Immune cells contribute to the maintenance of neurogenesis and spatial learning abilities in adulthood. *Nat Neurosci* 9:268–275.
43. Wadiche JI, Jahr CE (2005) Patterned expression of Purkinje cell glutamate transporters controls synaptic plasticity. *Nat Neurosci* 8:1329–1334.
44. Syken J, Shatz CJ (2003) Expression of T cell receptor beta locus in central nervous system neurons. *Proc Natl Acad Sci USA* 100:13048–13053.
45. Syken J, Grandpre T, Kanold PO, Shatz CJ (2006) PirB restricts ocular-dominance plasticity in visual cortex. *Science* 313:1795–1800.
46. Zohar O, et al. (2008) Cutting edge: MHC class I-Ly49 interaction regulates neuronal function. *J Immunol* 180:6447–6451.
47. Bryceson YT, Foster JA, Kuppusamy SP, Herkenham M, Long EO (2005) Expression of a killer cell receptor-like gene in plastic regions of the central nervous system. *J Neuroimmunol* 161:177–182.
48. Boulanger LM, Shatz CJ (2004) Immune signalling in neural development, synaptic plasticity and disease. *Nat Rev Neurosci* 5:521–531.
49. Schott E, Bonasio R, Ploegh HL (2003) Elimination in vivo of developing T cells by natural killer cells. *J Exp Med* 198:1213–1224.
50. Ziskin JL, Nishiyama A, Rubio M, Fukaya M, Bergles DE (2007) Vesicular release of glutamate from unmyelinated axons in white matter. *Nat Neurosci* 10:321–330.